CHAPTER 6

DESIGN AND SIMULATION INVESTIGATIONS OF DUAL-BAND (S- AND C-BAND) OF HIGH EFFICIENCY RBWO WITH BRAGG REFLECTOR DIRECT GENERATION OF GAUSSIAN PULSE

CONTENTS

CHAPTER 6: DESIGN AND SIMULATION INVESTIGATIONS OF DUAL-BAND (S-AND C-BAND) RBWO WITH BRAGG REFLECTOR FOR DIRECT GENERATION OF GAUSSIAN PULSE

6.1 Introduction

HPM oscillators like relativistic backward wave oscillator, reltron, magnetically insulated line oscillator (MILO), virtual cathode oscillator, relativistic klystron oscillator (RKO), relativistic magnetron, etc, have potential applications in high-power radar, plasma heating, nuclear fusion, nonlethal defence applications and so on. So far, HPM sources have been developed to generate high power with high efficiency in a single frequency band. In recent years, the dual frequency (either dual/bi frequency or dual band) HPM sources are being very attractive towards defense and radar applications. Currently, MILO and RBWO have been investigated at dual frequency or dual-band operation [42], [99]-[102]. Among all HPM sources, the relativistic backward wave oscillator is one of the most promising sources to generate microwave power at the gigawatt power level in both single frequency and multi frequency/band [1]. The dual-band frequency output RBWO has been investigated by several researchers but time-frequency generation and RF output power w.r.t drift section separating the cut-off section and Bragg structure, and Bragg structure and SWS are still a topic of research. The subassemblies of dual-band RBWO with Bragg reflector for TE_{11} mode output are the explosive emission cathode, cut-off neck section, drift section-1, Bragg reflector, drift section-2, SWS, and a tapered collector, as shown in Figure 6.1. The dual-band RBWO having TE_{11} mode output is more advantageous in view of compactness, as compared to a dual-band non-coaxial RBWO having TM_{01} mode, and dual-band coaxial RBWO having either TM_{01} or TEM mode. The upstream end of RBWO a Bragg reflector, which is a combination of both right and left single-fold-spiral corrugation, is

used as an interaction structure for the generation of another frequency spectrum at the output in addition to SWS. The Bragg reflector also acts as reflector to convert a backward TM01 mode into a forward TE_{11} mode with linear polarization at the output [2]-[4]. As a result, in spite of the existing complete operation of the dual-band RBWO with Bragg reflector for TE_{11} mode, there is a need to study in more detail about the RF output generation time and RF output power intended for operation with drift section length between the cut-off neck section and Bragg reflector, Bragg reflector and SWS, and the length of Bragg reflector.

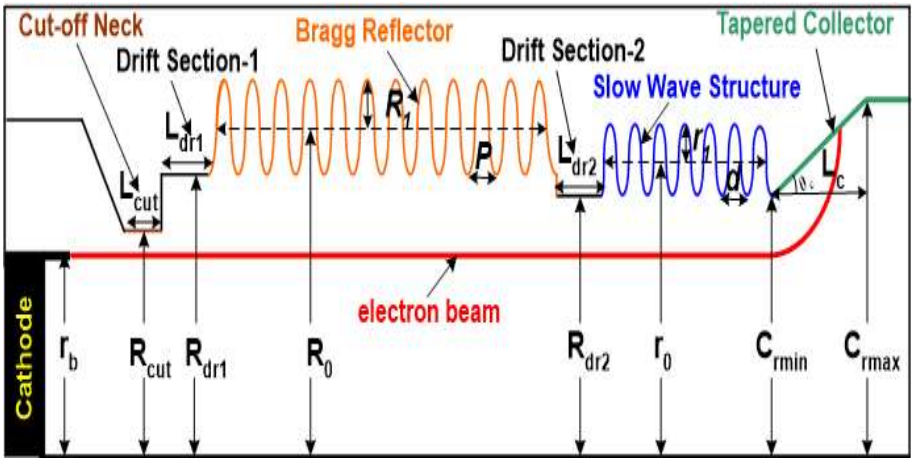

Figure 6.1: 2D Model of Dual-Band RBWO using Bragg Structure.

A new type of reflector, Bragg structure was introduced by Elfrgani et al. [97] and simulated a nine-period uniform RBWO with the twelve period Bragg reflector. The Bragg overcome the requirement of external mode converter but reduced the generating efficiency of the device. It has been more than a decade that researchers are extensively researching dual-frequency and dual-band HPM sources. In 1999, Yang et al. [98] experimentally demonstrated a two perpendicularly connected Cerenkov type oscillator (RBWO and OROTRON) operating at X-band and Q-band. Two perpendicular relativistic electron beams (REBs) emitted from the single accelerator and injected into RBWO and OROTRON, respectively. However, this method has a disadvantage of synchronism of beam and RF wave generated and not suitable

practically. In 2003, Ginzburg et al. [150] did a theoretical study of a dual-band RBWO with sectioned slow-wave structures (SWSs). Ting et al. [100] have demonstrated two dual-band RBWO structures through simulations. The first RBWO structure consists of two cascaded SWSs with single REB. The second RBWO structure consists of two parallel SWSs with dual IREBs. In 2012, Tang et al. [101] have demonstrated an X-band dual-frequency Coaxial RBWO with sectioned SWSs. A group at UNM worked for a direct generation of TE_{11} mode from an RBWO by using a Bragg structure as reflector and mode converter. A Bragg structure can play multiple roles like a reflector, a mode converter, and it can also act as an interaction circuit resonating at some frequency. In 2014, Elfrgani et al. [102] a dual-band RBWO having an uniform 9 periods SWS and 12 periods Bragg structure as an interaction circuit and reflector cum mode converter is demonstrated by MAGIC simulation. A two-way helically corrugated single fold Bragg structure is used that acts as an interaction circuit. However, the asymmetric mode and the helical corrugation reduced the overall efficiency of the device [102].

Thus, the design of a dual-band RBWO operated in both S- and C-bands with Bragg reflector and how the RF generation time and RF output power effected by the drift section separating the cut-off section and Bragg reflector, Bragg reflector and SWS, and length of the Bragg reflector are presented in this chapter.

6.2 Design Methodology of Bragg Reflector and Slow-Wave Structure

6.2.1 Design Methodology of Bragg Structure

In the present design, Bragg structure is used as both reflector cum mode converter, and it also acts as SWS to generate S-band frequency and reflect both dual-band (S-band and C-band) backward TM_{01} wave TE_{11} wave in the forward direction, *i.e.*, towards the

collector section. The schematic and 3D model of the Bragg structure is shown in Figure 6.2 [148, 149],

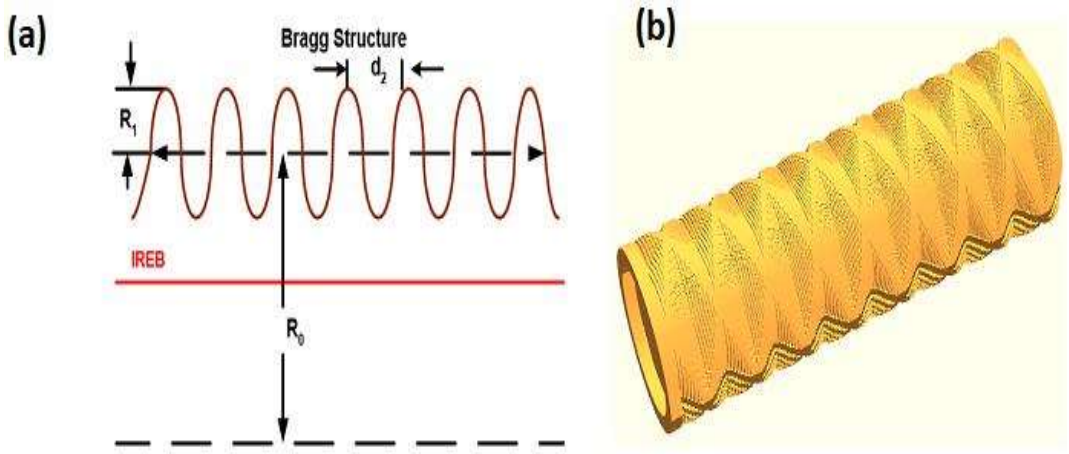

Figure 6.2: (a) 2D longitudinal cut view and (b) 3D model of Bragg Structure.

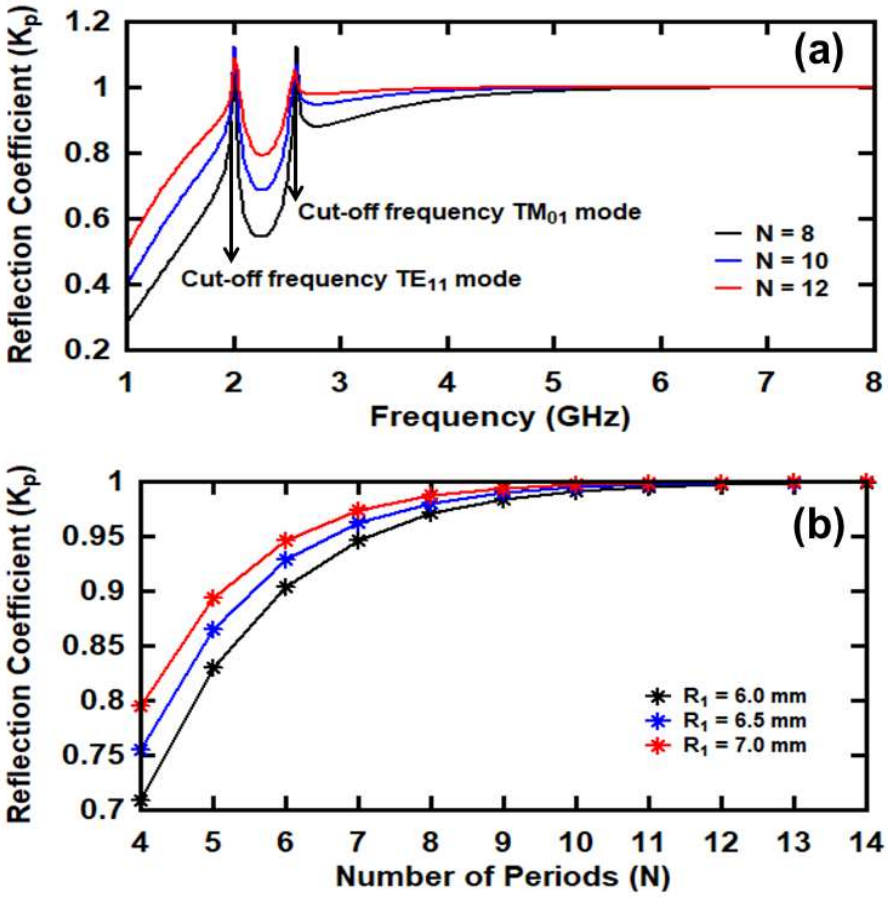

Figure 6.3: Reflection or conversion coefficient Vs (a) Frequency for different N and (b) number of Bragg axial periods for different corrugation depth (R1).

The detailed design of Bragg structure is already explained in Chapter 4.2. The coupling between TM_{01} and TE_{11} modes for the Bragg Structure is decided by the reflection coefficient [148], obtained by equation (4.10) and shown in Figure 6.3. It is observed from Figure 6.3 (a) that for the different number of Bragg periods and for fixed R1 = ~6.5 mm, the reflection or conversion coefficient is more than 99 % in S-band for N = 12. While Figure 6.3 (b) shows the variation of reflection or conversion coefficient with the number of Bragg axial periods for different values of corrugation depth and fixed frequency of 3.6 GHz. It is found that for R1 = ~6.5 mm the curve almost got saturated to one after N =12, hence the number of Bragg axial periods are chosen to be twelve for minimizing the losses. The calculated structural parameters of S-band Bragg structure are listed in Table 6.1shown below as explained in chapter 4.2.

6.2.1.1 Cold Simulation of Bragg Structure:

The main objective of using Bragg reflector in the present dual-band RBWO can be put in two folds: (i) mode conversion, and (ii) RF interaction structure (to generate RF output power in addition to slow-wave structure). The characteristics (S-Parameters) of mode conversion are observed by using cold simulation. 3D normal and cut view of the Bragg structure modelled in "CST Microwave Studio" is shown in Figure 6.4. To obtain the Bragg reflector's cold characteristics, at the end of the Bragg structure (Port 2 shown in Figure 6.4) TM_{01} mode is applied. The structure of Bragg reflector is designed with help of analytical face available in "CST Microwave Studio". The mathematical expression of is used in analytical face to model the corrugated sinusoidal profile. The major part of TM_{01} mode penetrates through the Bragg structure, and a minor part of TM_{01} is reflected due to the discontinuity in Bragg structure. The penetrated significant portion of TM_{01} is reflected from the entrance (Port 1 in Figure 6.4) of the Bragg

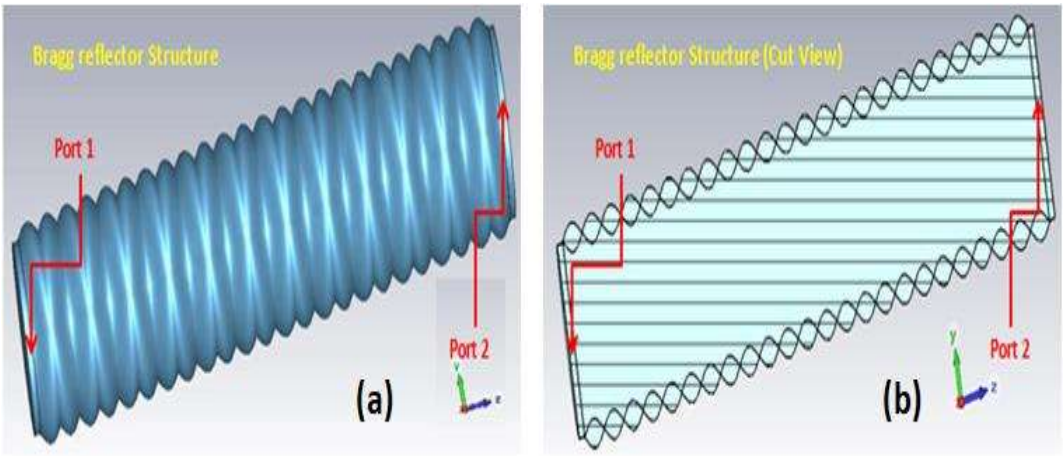

Figure 6.4(a): 3D View of Bragg reflector, and (b) 3D Cut view of Bragg reflector.

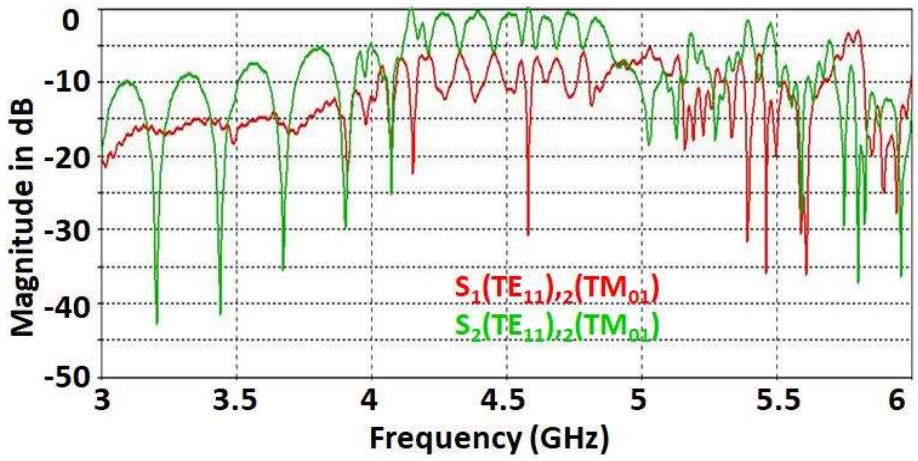

Figure 6.5: TM_{01} mode converted (reflected) from the end of Bragg reflector to TE_{11} mode to the end of Bragg reflector ($S2(TE_{11}),2(TM_{01})$), and the converted (reflected) TE_{11} mode penetration at the beginning of Bragg reflector ($S1(TE_{11}),2(TM_{01})$).

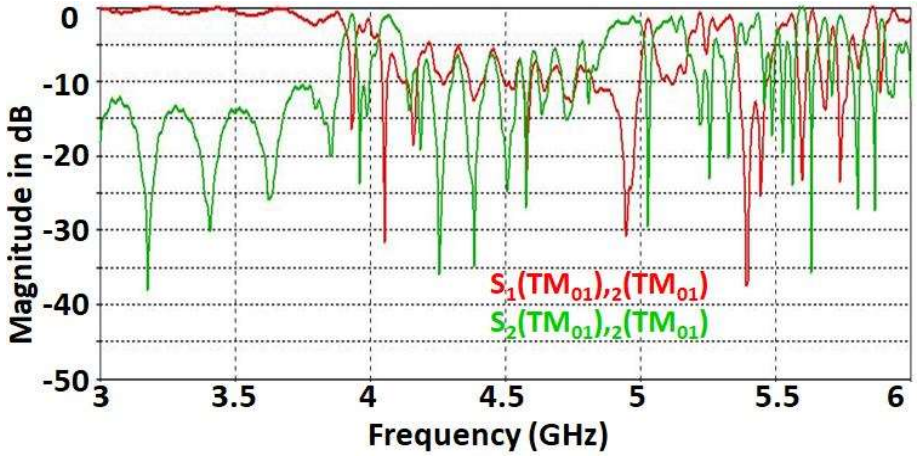

Figure 6.6: TM_{01} mode reflected from and to the end of Bragg reflector ($S2(TE_{01}),2(TM_{01})$), and TM_{01} mode penetration at the beginning of Bragg reflector ($S1(TE_{01}),2(TM_{01})$).

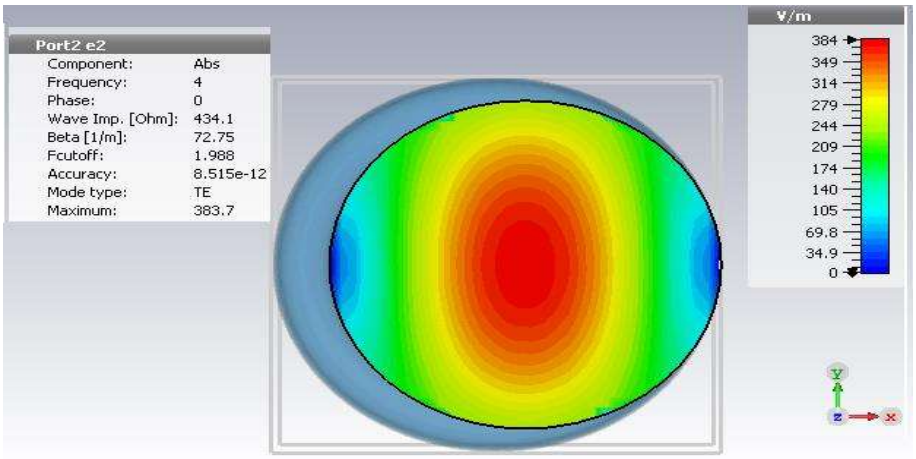

Figure 6.7: Mode pattern at the output port after mode conversion/reflection from TM_{01} at the output port (port 2), i.e., S2(TE_{11}),2(TM_{01}).

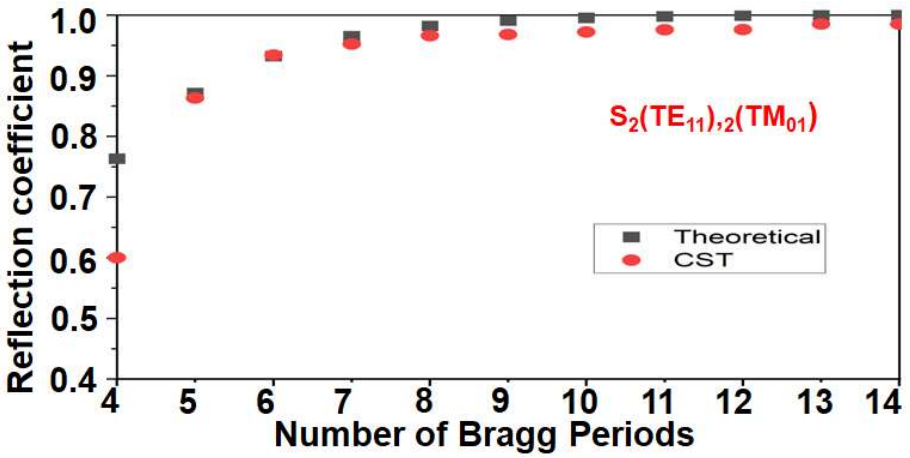

Figure 6.8: Validation of reflection coefficient Vs number of Bragg axial periods using analytical and simulation techniques.

reflector and converted into TE_{11} mode. The converted TE_{11} mode is forwarded towards the end of Bragg reflector (Port 2 in Figure 6.4). The reflection and mode conversion characteristics (S-parameters) of the Bragg reflector are shown in Figure 6.5 and Figure 6.5, with frequency band 4.0 GHz to 5.0 GHz respectively. The mode pattern obtained at the output port is also shown in Figure 6.7. It is observed that the output mode pattern at Port 2 is TE_{11} mode after the mode conversion/reflection from TM01 at the output port (Port 2), i.e., S2(TE11), 2(TM01). The power reflection coefficient is calculated with respect to the number of periods of Bragg structure and achieved a maximum reflection for N = 12, as shown in Figure 6.3 (b). The theoretically obtained results are

verified with CST cold simulation and found that both are in good agreement, as shown in Figure 6.8.

6.2.1.2 Cold Dispersion Diagram of BRAGG Structure

The dispersion relation of Bragg structure is explained in Chapter 4. 2. If $\delta_{E,H} = 0$ or negligible, equation (4.11) splits into two equations as for uncoupled TE_{11} and TM_{01} mode either $(k^2 - k_{\perp H}^2 - \bar{k}_H^2) = 0$ gives single assymtotic linefor TE_{11} mode – **Black Line** (Figure. 6.9) or $(k^2 - k_{\perp E}^2 - \bar{k}_E^2) = 0$ gives single assymtotic line for fundamental space harmonic TM_{01} mode – **Pink Line** (Figure 6.9) and also with $(k^2 - k_{\perp E}^2 - \bar{k}_E^2) = 0$, single assymtotic line for -1st space harmonic TM_{01} mode – **Blue Line** (Figure 6.9) can be drawn. Cold dispersion of the Bragg structure with nonzero couplings is divided into four roots, with two overlapping. If $\delta_{E,H} \neq 0$, equation (12) will give 4 roots (2 of roots get overlapped with each other) 2 roots – **Yellow line** (Figure 6.9) → TM_{01} undesired Eigen wave in Stop Band 2 roots – **Red line** (Figure 6.9) → TE_{11} desired Eigen wave in Pass Band. They are represented by the upper Eigen wave (W_{upper}) and lower Eigen wave (W_{lower}). The W_{upper} is in the stop band and the W_{lower} is in the pass band, which is

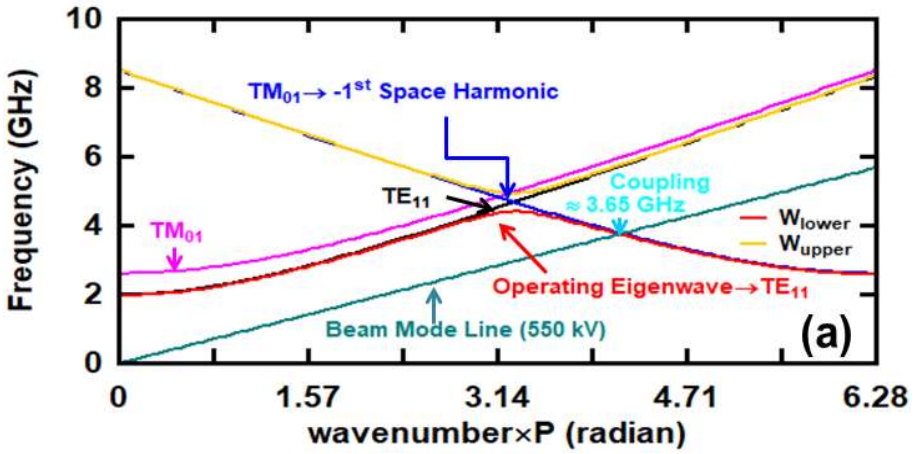

Figure 6.9: Dispersion diagram of Bragg structure.

the operating Eigen wave. The coupling of the desired TE_{11} mode and the -1st space harmonic of the TM_{01} mode is shown to be very close to the resonant frequency of the Bragg structure.

6.3 Slow Wave Structure (SWS)

6.3.1 Design Methodology

In the present design, the sinusoidal corrugation is considered [Figure 6.10] because of its smooth wall profile which helps in reducing the localized electric field at the sharped edges. The wall radius of the sinusoidally corrugated cylindrical waveguide depends on azimuthal (ϕ), radial (r) and axial (z) directions, which is described as,

$$r_w = r_0 + r_1 \sin(\bar{k}z + m\phi) \tag{6.1}$$

where, r_0 and r_1 is mean radius and corrugation depth, respectively, m is fold number, and $\bar{k} = 2\pi / d,$ d is the period of SWS, as shown in Figure 6.10.

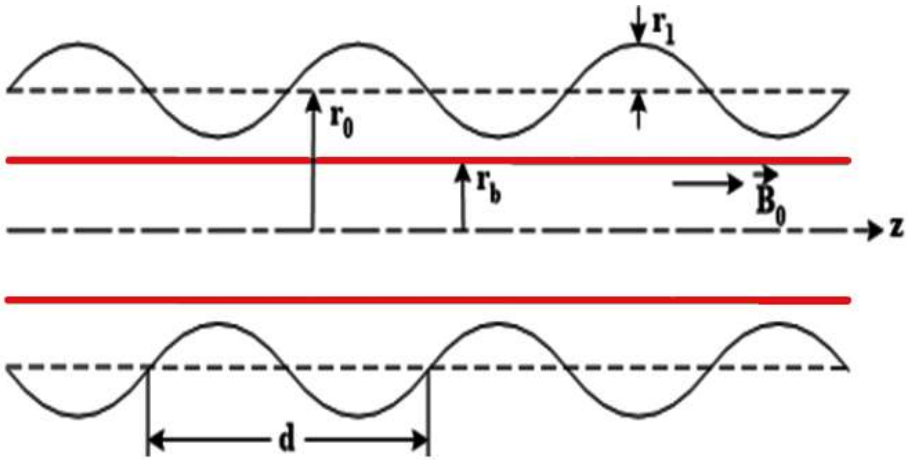

Figure 6.10: 2D Schematic of sinusoidal rippled wall SWS.

The SWS reduces the phase velocity of RF generated approximately equals to beam velocity. The SWS can have mean diameter (D) to free space wavelength ratio, *i.e.*, D/λ_r = 1 for conventional SWS. The design parameters are calculated as follows:

Mean radius (r_0): In the present C-band SWS design, D/λ value is chosen ~ 1.15, therefore at ~4.6 GHz, the mean radius is calculated as,

$$D/\lambda = (2*r_0) / \lambda \qquad [\lambda = c/f_1] \tag{6.2}$$

Therefore r_0 = 37.50 mm

The two radii, r_{max} and r_{min}, are such that

$$r_{\max} - r_{\min} \approx \frac{\lambda_r}{8} \tag{6.3}$$

The mean radius and corrugation depth are related to r_{max} and r_{min} as,

$$r_0 \approx \frac{r_{\max} + r_{\min}}{2} \tag{6.4}$$

$$r_1 \approx \frac{r_{\max} - r_{\min}}{2} \tag{6.5}$$

Ripple amplitude (r_1): This is also called as corrugation depth, which is chosen as, $\lambda/16 \le r_1 \le \lambda/8$. The value of ripple amplitude is chosen as, r_1=4.79 mm.

The period of SWS is calculated by equating the phase velocity of RF (v_{ph}) to the beam velocity (v_b) and is calculated by

$$v_{ph} \approx v_b \tag{6.6}$$

where,

$$v_{ph} = \frac{2\pi f_r}{k_z}, \text{ and } v_b \approx c\sqrt{1 - \frac{1}{\gamma_b^2}} \tag{6.7}$$

where, γ_b is the relativistic factor under the influence of space charge effect [17], k_z is π/d for π-mode of operation which will explained in detail later, thus substituting

this value in (6.6) and (6.7), we get

$$2df_r \approx v_b \tag{6.8}$$

where, v_b is calculated using $\gamma_b = \frac{1}{\sqrt{1-(v_b/c)^2}}$. The value of γ_b (beam factor) is calculated by using the beam current, which is given as,

$$I_b = \frac{I_A}{2\ln(r_o/r_b)}\left(\gamma_b^2-1\right)^{1/2}\frac{\gamma_c-\gamma_b}{\gamma_b}[\mathrm{kA}] \tag{6.9}$$

where, $\gamma_c = 1+\left|eV/mc^2\right|$ is Lorentz factor, and r_b is the beam radius. From equation (6.9), we can note that when $\gamma_b = 1$ and $\gamma_b = \gamma_c$ the beam current I_b=0, and when $\gamma_b = \gamma_c^{1/3}$ the maximum allowable steady-state current (I_{scl}) is obtained, as shown in Figure 6.11 (a).

$$I_{scl} = I_{\lim} = \frac{I_A}{2\ln(r_o/r_b)}\left(\gamma_c^{2/3}-1\right)^{3/2}[\mathrm{kA}] \tag{6.10}$$

where, $I_A = 4\pi\varepsilon_0 mc^2/e = 17.1\,\mathrm{kA}$. The I_{scl} is the maximum steady-state current that the waveguide can handle, which is referred to as the space-charge- limiting current. A complication arises because γ_b is a double valued function of I_b. The low-energy/high-charge density branch with $1 \le \gamma_b < \gamma_c^{1/3}$ has the higher total energy for given I_b, however, so we will limit the high-energy/low-charge density branch with the assumption that this is a physically preferable state.

The value γ_b is calculated from the equation (6.9) by using r_0, r_b ,V_0, and γ_c by choosing the beam current as I_b=5.9 kA (Figure 6.11 (b)), r_b/r_0 = 0.72 and beam voltage

V_0 = -550 kV. From Figure 6.11 (a), γ_b = 1.78 at 5.9 kA is chosen and substituted in equation (6.8) that gives, v_b = 0.82c. The plot of I_b Vs γ_b for V_0 = 550 kV and different values of r_b/ r_0 is shown in Figure 6.11 (a). The plot of I_{scl} Vs V_0 for different values of r_b/r_0 is also shown in Figure 6.11 (b). The value r_b/r_0 = 0.72 is chosen good beam-wave interaction for the beam voltage V_0 = 550 kV. Substitute f_l=4.6 GHz and v_b in equation (6..8), therefore $d \approx 27.82$ mm.

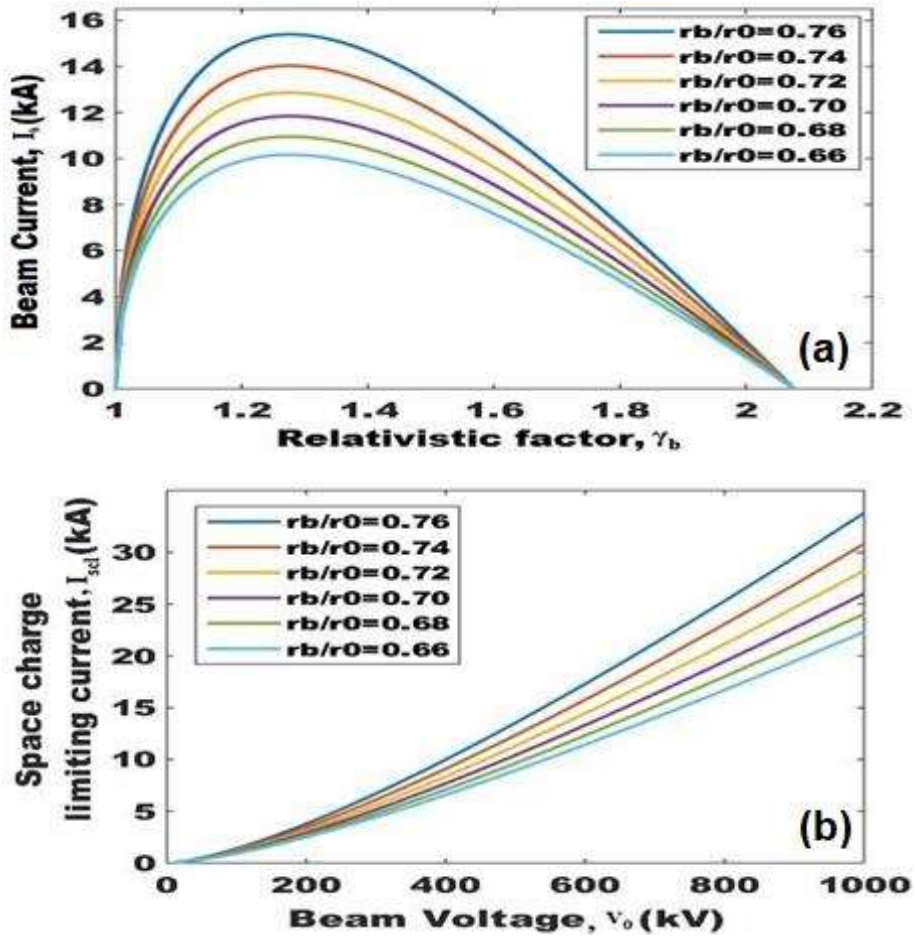

Figure 6.11: (a) Dependence on beam current I_b on γ_b and (b) Dependence on beam current I_{scl} on V_0 for different r_b/r_0.

6.3.2 Cold Dispersion Diagram of Slow Wave Structure

The dispersion diagram of the C-band corrugated SWS analyzed using equation (2.45) as shown in Figure 6.12 It is observed that the beam mode line corresponding to the

beam voltage 550 kV intersects with the operating mode line at ~4.6 GHz and coupling of -1st space harmonic of TM_{01} mode. The beam mode line intersects TM_{01} mode line having a negative slope which shows that the RF wave generated has the negative group velocity.

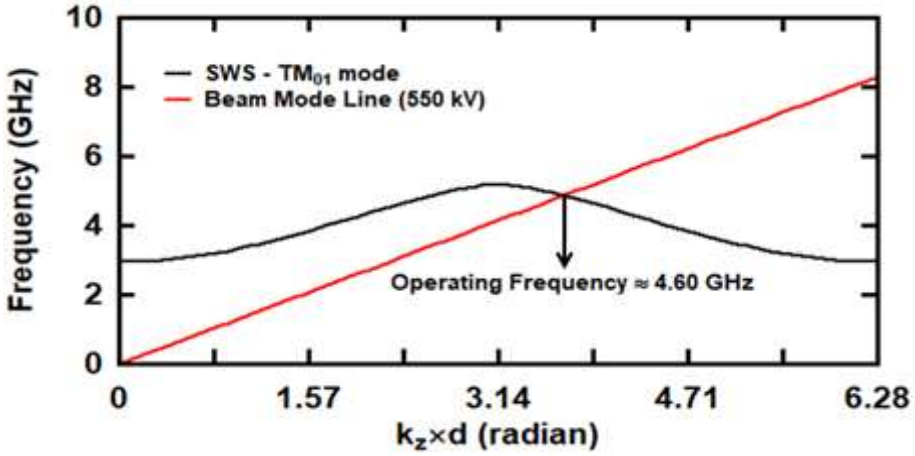

Figure 6.12: Dispersion diagram for SWS in C-Band.

6.4 Cut-off Neck Reflector and Drift Sections

The radius of the reflector is calculated in such a way that it should have a cut-off frequency more than the operating frequency of backward propagating wave such that the backward propagating mode become forward propagating mode and values are calculate by [18], [19] equation (2.6) as explained in chapter 2.3.2.

The drift section-1 and drift section-2 (Figure 6.14) having the cut-off frequency ($\chi_{01}c / 2\pi f_1 \leq R_{dr1,2} < \chi_{02}\, c/ 2\pi f_1$ for f_1=3.6 GHz) more than the operating frequency of SWS (C-band) and Bragg reflector (S-band) to enhance the reflection of backward propagating TM_{01} mode to forward propagating linearly polarized TE_{11} mode and protect the wave propagation towards the cathode. In the present design, the maximum RF output power is obtained for L_{cut}= 4.80 mm, L_{dr1}= 18.00 mm, and L_{dr2}= 15.80 mm of both bands.

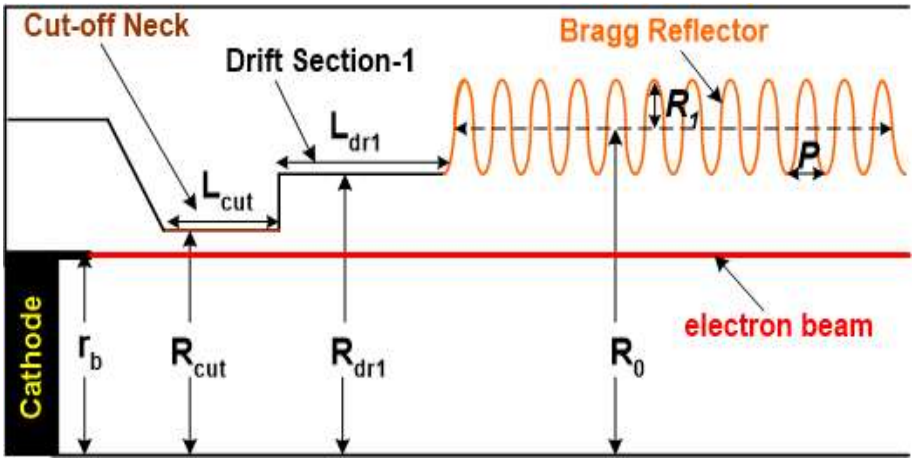

Figure 6.13: 2D schematic shows cathode, cut-off neck reflector and drift Section-1.

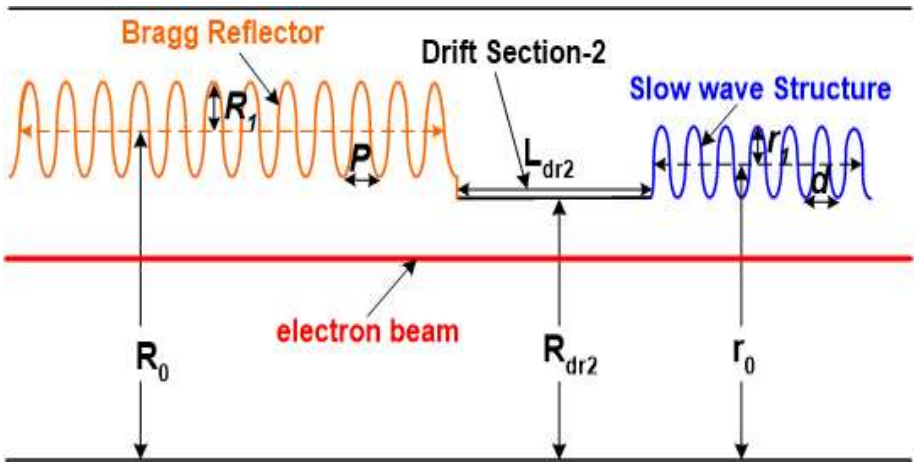

Figure 6.14: 2D schematic of drift Section-2 separating Bragg and slow wave structures.

6.5 Tapered Waveguide Collector

The tapered waveguide collector as shown in Figure 6.15. In the present design, the up-

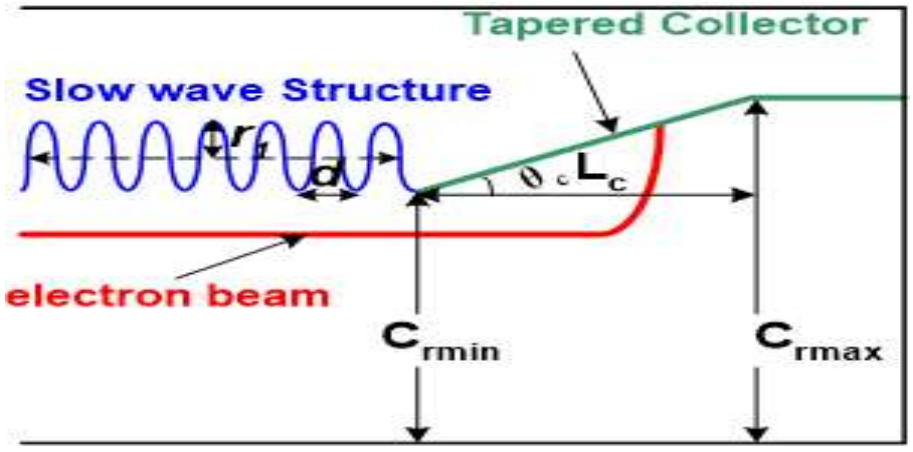

Figure 6.15: 2D schematic of tapered collector section.

taper angle θ_c=7.9^0 and length of the up-taper is L_c = 75.10 mm are chosen as explained in chapter 2.3.4.

The complete design (structural and electrical) parameters of the present dual-band RBWO with Bragg structure operating in S- and C-band is given in Table 6.1.

Table 6.1: Optimized Design Parameters of Dual-Band RBWO using Bragg Reflector.

Parameters		**Symbol**	**Value**
Bragg Structure (m=±1)	Bragg Mean radius	R_0	44.12 mm
	Bragg Ripple amplitude	R_1	06.45 mm
	Bragg Period	P	37.78 mm
	Bragg length	L_{Bragg}	12*P mm
	Bragg operating Frequency	f_1	~3.55 GHz
Slow Wave Structure (SWS)	SWS Mean radius	r_0	38.99 mm
	SWS Ripple amplitude	r_1	4.79 mm
	SWS Period	d	28.20 mm
	SWS length	L_{sws}	6*d mm
	SWS Operating frequency	f_2	4.42 GHz
Cut-off Neck Section	Length	L_{cut}	4.80 mm
	Radius	R_{cut}	33.40 mm
Drift Section-1	Length	L_{dr1}	18.00 mm
	Radius	R_{dr1}	37.67 mm
Drift Section-2	Length	L_{dr2}	15.50 mm
	Radius	R_{dr2}	33.77 mm
Tapered Collector	Collector Length	L_c	85.00 mm
	Inner Radius	$r_{c,min}$	34.22 mm
	Outer Radius	$r_{c,max}$	45.22 mm
Cathode	Beam Radius	R_b	32.18 mm
Electrical Parameters	Input voltage	V_0	550 kV
	Beam current	I_0	~5.95 kA
	Magnetic field	B_0	1.3 T

6.6 PIC simulation of Dual band RBWO

In the present design, a Bragg structure is modeled and added in between the drift section-1 and drift section-2. The addition of Bragg structure with RBWO is to generate microwave power directly in TE_{11} output mode. A two-way (left and right) single-fold helically corrugated structure having 12 uniform axial periods with sinusoidal profile is used for the beam-wave interaction. One helical corrugation converts the backward propagating TM_{01} mode into a left-circular TE_{11} mode, while the other helical corrugation converts the backward propagating TM_{01} mode into a right-circular TE_{11} mode and the resultant is the linearly polarized TE_{11} mode. The corrugated sinusoidal profile of Bragg and SWS are created using FUNCTIONAL VOLUME command available in MAGIC-3D. Finally, two drift sections and one cut-off section are modeled by using the conformal volume command 'VOLUME' as shown in Figure 6.16. The drift section-1 is modeled in between the cut-off neck section and Bragg structure, and the drift section-2 is modeled in between Bragg structure and SWS. The cut-off section is modeled before the drift section-1. Both drift section-1 and drift section-2 help to improve the synchronization condition between the slow space charge wave associated with the beam of TM01 (S-band and C-band) and RF wave. The cut-off frequency ($R_{cut} \approx \chi_{mn} c / 2\pi f_c$) of cut-off neck section, and the cut-off frequency ($\chi_{01} c / 2\pi f \le R_{dr} < \chi_{02}$ c/ $2\pi f$) drift section-1 and drift section-2 are more than the operating frequency of SWS (C-band) to enhance the reflection of backward propagating TM_{01} mode into forward propagating linearly polarized TE_{11} mode and also to protect the wave propagation towards the cathode.

The annular cathode is made to generate an IREB by the explosive emission process, and electron emission occurs from the cathode when the electron beam energy 550 keV

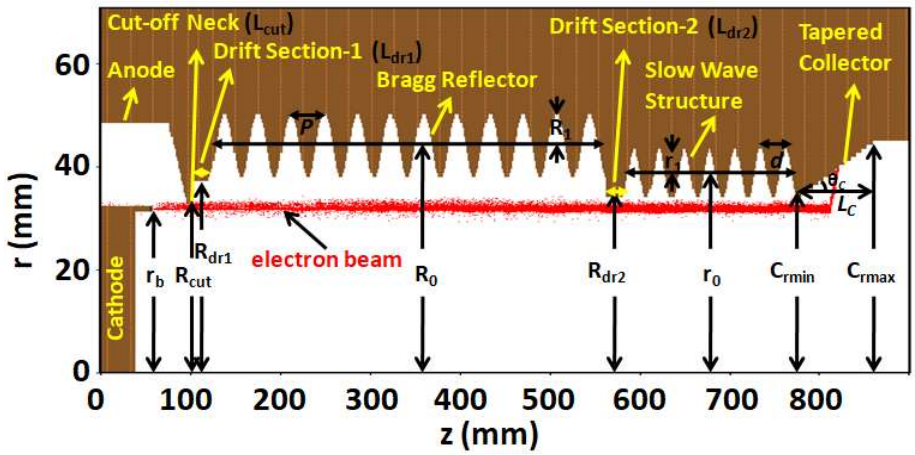

Figure 6.16: 2D Model simulation structure of Dual-band RBWO with Bragg reflector under guiding magnetic field 2.0 T and DC input voltage 550 kV.

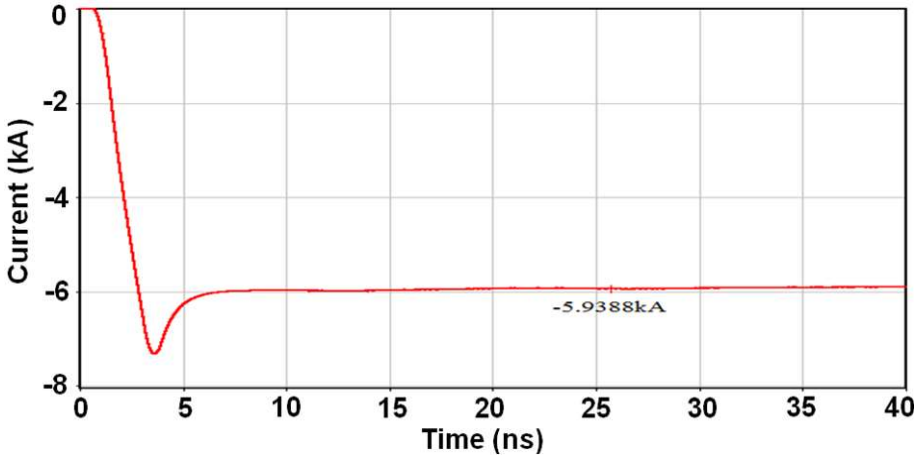

Figure 6.17: Developed electron beam current.

is applied to the anode-cathode gap. The electron beam travels through the interaction structure and transfer its energy to the -1[st] harmonic of the backward TM_{01} wave when a strong guiding magnetic field of 2.0 T applied in the axial direction of the structure. The developed beam current for the given annular cathode parameters is shown in Figure 6.17. In the present design, the magnetic fields at the cyclotron resonance are calculated as, $B_1 \sim 0.15$ T and $B_2 \sim 1.16$ T ($d = 28.20$ mm, and $\gamma_b \approx 1.8$) by using equations (2.25) and (2.26) , respectively. For $v_b \approx 0.82\ c$ (from equation 6.20) is the electron longitudinal velocity, and $k_z = \sqrt{(\omega/c)^2 - (\chi_{mn}/r_0)^2}$ (χ_{mn}=1.814 for TE_{11} mode, r_o= 38.99 mm. Therefore, k_z = 84.37 mm) is the fundamental spatial harmonics of longitudinal

wavenumber. The two unwanted cyclotron synchronism resulted in the suppression of output RF power.

The PIC simulation of a dual-band RBWO using Bragg structure is performed using the commercially available 3D electromagnetic code "MAGIC-3D". The instantaneous RF output power is shown in Figure 6.18. It is calculated at the end port area of the device with OBSERVE FIELD_POWER S. DA command. An average RF output power of ~600 MW (Figure 6.19) is calculated at the device's end port area with OBSERVE FIELD_POWER S. DA FILTER STEP command. The corresponding operating frequency is calculated by the command OBSERVE FIELD_INTEGRAL E.DL at the end of the simulation and applying the Fast Fourier Transform (FFT) with a

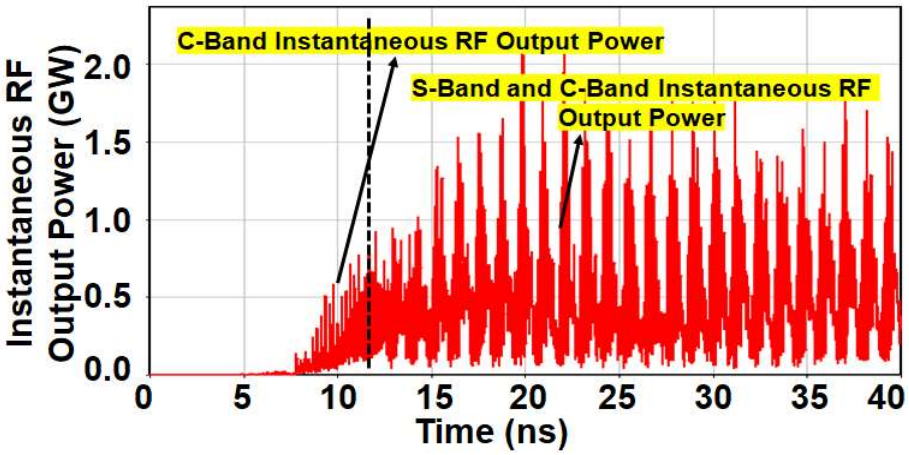

Figure 6.18: Instantaneous RF output power.

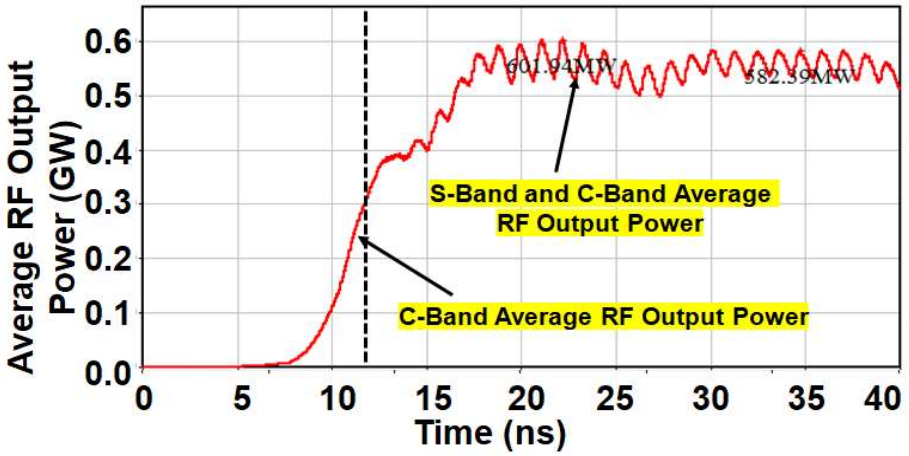

Figure 6.19: Average RF output power with DC input voltage 550 kV.

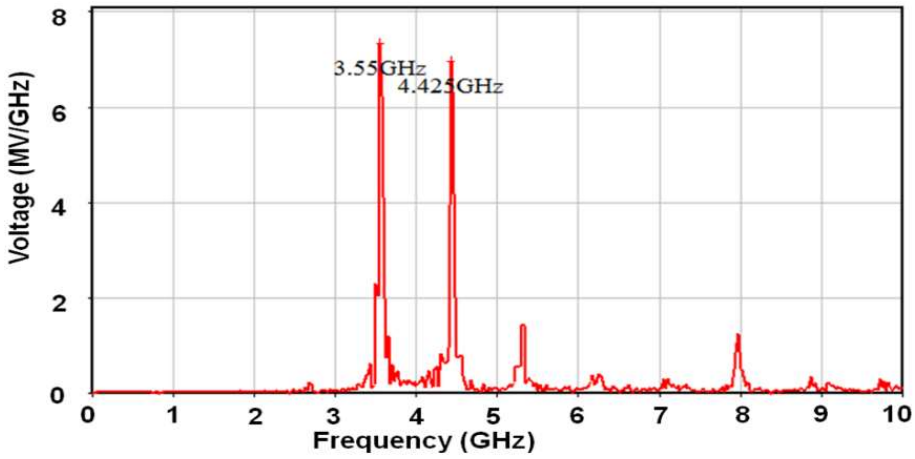

Figure 6.20: FFT of the generated HPM wave for dual-band frequency.

frequency window from 0 to 10 GHz. The simulation predicted two frequencies, which are ~3.55 GHz and 4.42 GHz (Figure 6.20).

The evolution of all particle's energy distribution with the function of axial distance at different instances of time is shown in Figure 6.21, which shows that the electron bunching process in both SWS and Bragg reflector of the dual-band RBWO. The particle energy moving from the cathode end and terminated at the collector dump location. The bunching process starts initially from the end of SWS and ended at the beginning of Bragg structure. It indicates that the bunched electron beam losses its energy from the end of SWS and ended at the beginning of Bragg reflector. Therefore, the electron beam is initially interacted with SWS and generated an RF output power at ~4.5 GHz, and after some time the electron beam is interacted with Bragg reflector and generated an RF output power at ~3.6 GHz. The difference in the RF output power generation time clearly observed in the time-frequency evolution of electric field, as shown in Figure 6.22 for the obtained dual-band RF output power. The frequency spectrum and time-frequency plots show that there is no mode competition, and no harmonic generation is observed in the device for the entire simulation time. From Figure 6.22, it is observed that the RF generation in S-band at ~3.55 GHz is started at

~12.50 ns, and the RF generation in C-band at ~4.42 GHz is started at ~8 ns. The difference in the generation time due to (Figure 6.22) difference in start current of S-and C-band. The start current of the C-band is less than the S-band. The contour plots show the output mode pattern at different time instances of the hot- simulation time, as shown

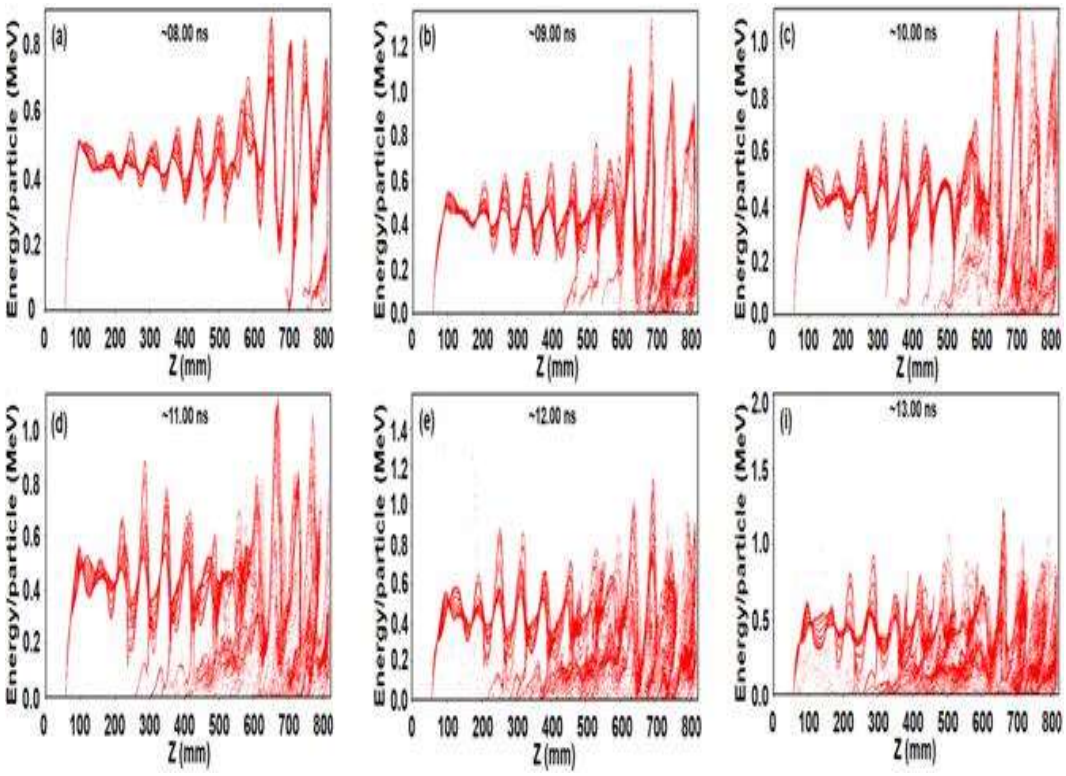

Figure 6.21: Particle energy distribution with the function of axial direction at different instances of time.

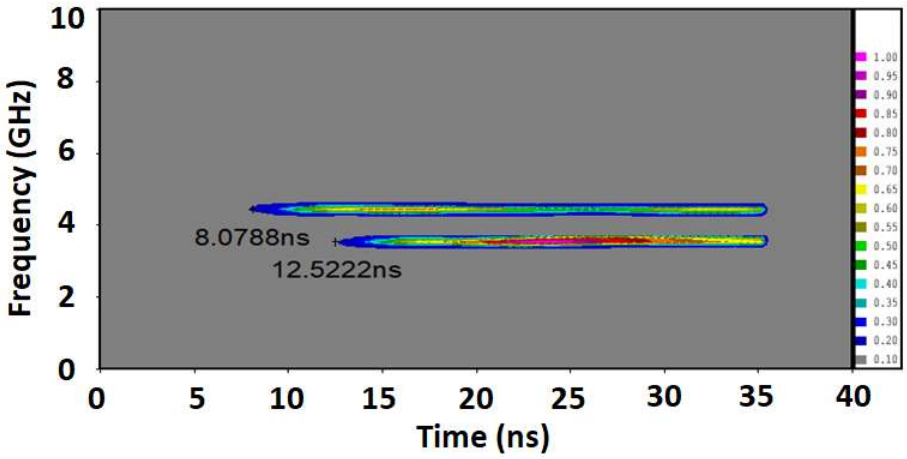

Figure 6.22: Time-Frequency plot showing generation of dual-band frequencies.

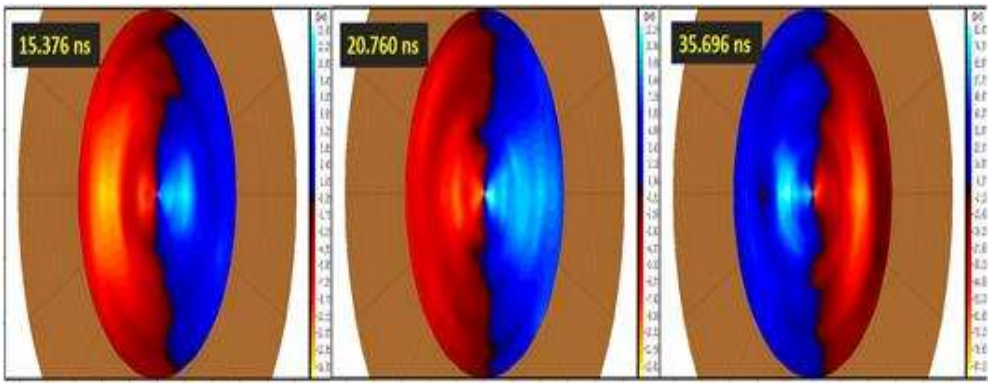

Figure 6.23: Contour plots of the radial electric field showing linearly polarized TE_{11} generated mode shown at a different simulation time.

in Figure 6.23. It is observed from Figure 6.23 that the RBWO has two-way (left and right) helically corrugated single fold (m = 1) cylindrical waveguide outputted the linearly polarized TE_{11} mode for both S- and C-bands, respectively.

6.7 Parametric Analysis

In this section, the sensitivity of the device with the magnetic field is studied on average RF output power, frequency, and efficiency.

6.7.1 Effect on frequency and average RF output power with magnetic field.

In the present configuration, the RF generation is suppressed in region (i) due to cyclotron absorption [Figure 6.24 (a)]. However, the RF generation is not suppressed in region (ii) due to Cherenkov absorption, which does not occur simultaneously in both S- and C-band [Figure 6.24 (a)]. Therefore, the RF power is continuously generated even if any one of the bands is under Cherenkov absorption [Figure 6.24 (b)]. The dual-band frequency generation and average RF output power were observed by varying the magnetic field from 0.0 T to 2.0 T (Figure 6.24). The dual-band RF generation is commenced from ~0.22 T [Figure 6.24 (a)] and below that value, the dual-band RF generation is absent due to cyclotron absorption. Further, the S-band generation is absent from 0.27T to 0.55 T, and the C-band generation is absent from 0.42 T to 0.78 T

[Figure 6.24 (a)], which is caused by Cherenkov absorption. The simulation of Cherenkov and cyclotron absorption of magnetic field values are good in agreement with theoretical values, as explained in equations (2.21) and (2.22), respectively [125]. The dual-band frequency generation with high RF output power consists of time-frequency generation up to 60 ns simulation time (Figure 6.19, Figure 6.20, and Figure 6.21) is achieved at 1.3 T as shown in Figure 6.24 (b).

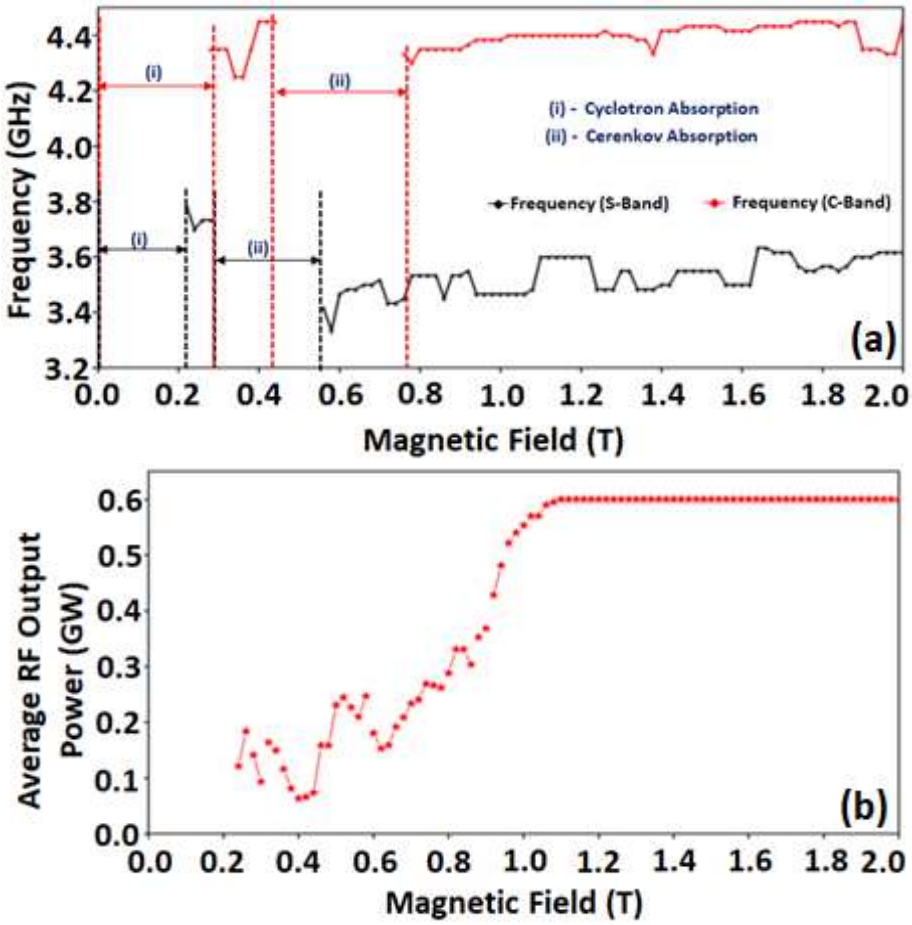

Figure 6.24: Effect of guiding magnetic field on (a) Dual-band frequency generation and (b) Average RF output power.

6.8 Conclusion

The time-frequency generation performance of the dual-band RBWO with Bragg reflector has been investigated for different length of the drift section-I, drift section-II, and length of the Bragg reflector. The cathode parameters of beam voltage 550 kV applied and beam current 5.4 kA developed in the device. The RF output power ~600

MW generated at ~3.6 GHz and ~4.5 GHz. the RF generation time are ~12.00 ns (~3.6 GHz) and ~09.00 ns (~4.5 GHz) obtained. The conversion efficiency for both frequencies is 18.50 % with guiding magnetic field of 1.3 T. Additionally, it is also capable of generating TE_{11} mode at output end with the advantageous of Bragg reflector. The frequency tuning observed by changing the length of drift section-I and drift section–II without much affect the RF output power. The effect of RF generation time and RF output power observed by changing the length of drift section-I and drift section–II. The effect of Bragg reflector length also affects the dual-band frequency generation.

Further, the dissertation is concluded with its future scope in the next Chapter.